Biomass Derived N-doped Porous Carbon Made from Reed Straw for Enhanced Supercapacitor

Yuyi Liao , Zhongtao Shang , Guangrui Ju , Dingke Wang , Qiao Yang , Yuan Wang * , Shaojun Yuan *

Posted Date: 18 May 2023

doi: 10.20944/preprints202305.1311.v1

Keywords: Biomass; Supercapacitors; Nitrogen doping; Melamine; Porous Carbon

Article

Biomass Derived N-Doped Porous Carbon Made From Reed Straw for Enhanced Supercapacitor

Yuyi Liao, Zhongtao Shang, Guangrui Ju, Dingke Wang, Qiao Yang, Yuan Wang * and Shaojun Yuan *

Low-carbon Technology & Chemical Reaction Engineering Lab, College of Chemical Engineering, Sichuan University, Chengdu 610065, China.; yimilyymail@163.com (Y.L.); taozi11281125@163.com (Z.S.); jugr0013@163.com (G.J.); dingkew0506@163.com (D.W.) yangqiaomail@163.com (Q.Y.)

* Correspondence: wangyuan2022@scu.edu.cn (Y.W.)l ysj@scu.edu.cn (S.Y.)

Abstract: Developing advanced carbon materials by utilizing biomass waste has attracted much attention. Herein, a N-doped carbon material (RSM-0.33-550) was prepared by directly pyrolyzing reed straw and melamine. The as-prepared RSM-0.33-550 possessed a N content of 6.02% and a specific surface area of 547.1 m^2 g^{-1}. As the anode for supercapacitors (SCs), in 6 M KOH, such RSM-0.33-550 exhibited a capacitance of 202.8 F g^{-1} at a current density of 1 A g^{-1}. At a high current density of 20 A g^{-1}, it still remained a capacitance of 158 F g^{-1}. Notably, it delivered an excellent stability with capacity retention of 96.3% at 20 A g^{-1} after 5000 cycles. This work not only offer a new electrode material for SCs, but also gives a new insight for rationally utilizing the biomass waste for energy storage.

Keywords: biomass, supercapacitors, nitrogen doping, melamine, porous carbon

1. Introduction

Nowadays, the world is facing a series of problems caused by fossil fuel combustion [1]. It is urgently to develop the energy storage devices (EESs) by utilizing clean and sustainable energy (wind, solar, and tidal energy, etc) [2,3]. Electric double-layer capacitors (EDLCs) exhibit high specific power (up to 10 KW kg^{-1}), fast charge/discharge capability, and long cycle life (e.g. millions of cycles), has attracted much attention [4,5]. However, EDLCs contain porous carbon electrodes that presents the charge storage mechanism of ion adsorption at the electrolyte and electrode interface, and no electrochemical reactions are involved [6,7]. This is responsible for the EDLCs poor energy content [8]. Therefore, it is necessary to improve the porous carbon material to enhance the faradaic reaction for promoting the specific capacitance.

Biomass carbon material is a carbon-rich solid produced as a by-product from the thermochemical pyrolysis of biomass in an oxygen-limiting environment, which can serve as the electrode for supercapacitors (SCs) [9–11]. The chemical and physical properties of biomass carbon vary significantly with the feedstock and fabrication conditions [12,13]. Their carbonized network can provide a more surface area and give the ion diffusion pathway for charge storage. Momodu et al. synthesized activated carbon derived from bark through a simple activation and carbonization process, it showed a capacitance of 191 F g^{-1} at 1 A g^{-1} [14]. Kesavan et al. fabricated nitrogen-doped carbon nanosheets using peanut shell as a precursor. At a current density of 1 A g^{-1}, a capacitance of 195 F g^{-1} can be achieved [15]. A Alpinia officinalis leaf derived porous carbon was reported by Taer et al., and it delivered a capacitance of 161 F g^{-1} at 1 A g^{-1} [16]. Kang et al. prepared hierarchical porous carbon materials using peanut bran as raw material through hydrothermal carbonization and KOH activation reaction, and a capacitance of 188 A g^{-1} was reached at 0.04 A g^{-1} [17]. Reed straw is a rich biomass material with rich cellulose, lignin, and hemicellulose [18]. The reed straw derived porous carbon is considered as the promising candidate for charge storage [19]. Such hollow structure can provide more interface of solid-liquid interface for EDLC.

 doi:10.20944/preprints202305.1311.v1

Until now, various natural biomass materials such as bacterial cellulose [20], orange peels [21], rice stems [22], bamboo [23], and carb shell [24] have been reported as the precursors to prepared carbon anode for SCs. These biomass carbon materials based no EDLC charge storage mechanism can be improved by increasing their surface area. However, the increased surface area contributing EDLC is limited, and the capacitance and energy density of carbon materials usually remain poor [11]. Recently, the introduction of electrochemical-active functionalities (e.g., O, N, P, and S containing groups) on the carbon skeleton turned out to be a feasible approach to significantly boost the capacitance of carbon-based SCs [25–28], especially nitrogen doping of carbon, which can increase the surface polarity, electric conductivity, and electron-donor affinity for carbon network. The capacitance of nitrogen-doped carbons (NPCs) comes from not only EDLC but also the faradaic reaction at or near in the surface of carbon material [29]. Generally, the preparation of NPCs is achieved through the pyrolysis of biomass waste containing N element, and the post-treatment of carbon materials with ammonia and urea at high temperatures [30]. Therefore, we anticipated that pyrolyzing the reed straw with N-containing organic to fabricate the porous carbon materials with rich active sites, which can serve as the electrode for boosting SCs.

In this work, a reed straw derived biomass carbon (RSM) was prepared by directly pyrolyzing reed straw and melamine with KOH as the activator. The RSM as the electrode for SCs exhibited an enhanced electrochemical performance with rationally introducing melamine. In addition, the pyrolysis temperature was taken into considered. The optimized RSM-0.33-550 (the mass ratio of melamine to reed straw is 1 : 3 and the optimal activation temperature is 550 °C) with a N content of 6.02% and a specific surface area of 547.1 m^2 g^{-1} displayed a capacitance of 202.8 and 164 F g^{-1} at a current density of 1 and 20 A g^{-1}, respectively. At a high current density of 20 A g^{-1}, it still remained a capacitance of 158 F g^{-1}. It also showed an outstanding stability with capacity retention of 96.3% at 20 A g^{-1} after 5000 cycles.

2. Experimental Section

2.1 Materials and Methods

Reed straw powder (60 mesh) purchased from Shaanxi Jinhe Agricultural Technology Co., Ltd. Melamine and potassium hydroxide (KOH) were purchased from Shanghai Aladdin Biochemical Technology Co. (Shanghai, China). Polyvinylidene fluoride (PVDF), acetylene black, concentrated hydrochloric acid (HCl), N-methylpyrrolidone (NMP), and other chemical reagents were purchased from Chengdu Kelong Chemical Reagent Co. (Chengdu, China). Nitrogen was purchased from Guangdu Gas Business Department (Chengdu, China). All reagents were analytical grade and used as received without any further purification.

2.2 Preparation of RSM-y-550

2 g of reed straw powder was mixed with varying weights of melamine (0 g, 0.66 g, 2 g, and 6 g), and stirred continuously after adding 50 mL deionized water, then transferred to a 75 mL Teflon stainless steel autoclave and reacted in an oven at 120 °C for 2 h. When cooled to room temperature, a yellowish powder (RSM) is obtained. Subsequently, 1 g of RSM powder and 1 g of KOH were added in 10 mL deionized water with continuously stirring for 4 h, and then dried at 80 °C for 12 h. The mixture is transferred in a porcelain boat and putted in a tubular furnace for further activation. The activation operation was conducted at 550 °C for 2 h, with the temperature raise rate of 5 °C min^{-1} under nitrogen atmosphere to obtain a porous carbon. Then it was cleaned with 1 M hydrochloric acid and washed with deionized water for several times, and dried by vacuum at 60 °C for 12 h. The obtained sample was denoted as RSM-y-550, where y represents the mass ratio of melamine to reed straw (y = 0, 0.33, 1, and 3).

2.3 Characterization

XRD patterns were collected on an X-ray diffractometer (Philip Company, Pw1730) equipped with a Cu Kα radiation (λ = 1.5418 Å). XPS spectra were measured on an X-ray photoelectron

Preprints (www.preprints.org) | NOT PEER-REVIEWED | Posted: 18 May 2023 doi:10.20944/preprints202305.1311.v1

spectroscopy spectrometer (XPS, a Kratos Axis Ultra spectrometer, Kratos Analytical Inc. Manchester, UK). SEM images were captured on a Hitachi S-4800 field emission scanning electron microscope (Hitachi High-Tech Co., Tokyo, Japan) at an accelerating voltage of 20 kV. Raman spectra were measured on a DXR Raman microscope (Thermo Fisher Scientific Inc., Waltham, MA, USA) with an excitation wavelength of 455 nm. Brunauer-Emmett-Teller (BET) surface area was collected on a Micromeritics TRISTAR II3020 surface area analyzer (Micromeritics Instrument, Norcross, GA, USA).

2.4 Electrochemical Measurement

To prepare the RSM-y-550 working electrode, the prepared mixture of active carbon material (80 wt%), polyvinylidene fluoride (10 wt%), and acetylene black (10 wt%) were coated on nickel foam (1.0 × 1.0 cm^2) and dried at 80 °C for 24 h. The three-electrode system was employed to estimate the electrochemical performance of all electrodes. RSM-y-550 was used as the working electrode (anode), with platinum as the opposite electrode, saturated calomel electrode (SCE) as the reference electrode, and 6 M KOH solution as the electrolyte. Cyclic voltammetry (CV), galvanostatic charge-discharge (GCD) and electrochemical impedance spectroscopy (EIS) were performed at CHI600E electrochemical workstation (Chenhua Instrument Co., Shanghai, China). The GCD was employed at a current density of 1–10 A g^{-1}. The CV was conducted at a scan rate of 10–100 mV s^{-1}. The frequency range of EIS was 0.01–100 kHz, and the potential window was 5 mV. According to the results of GCD curve, the capacitance is calculated as follows: $C = I \times \Delta t / (m \times \Delta V)$, where ΔV (V) is the potential window, m (g) is the mass load of the active substance, Δt (s) is the discharge time, I (A) is the current density, C (F g^{-1}) is the specific capacitance.

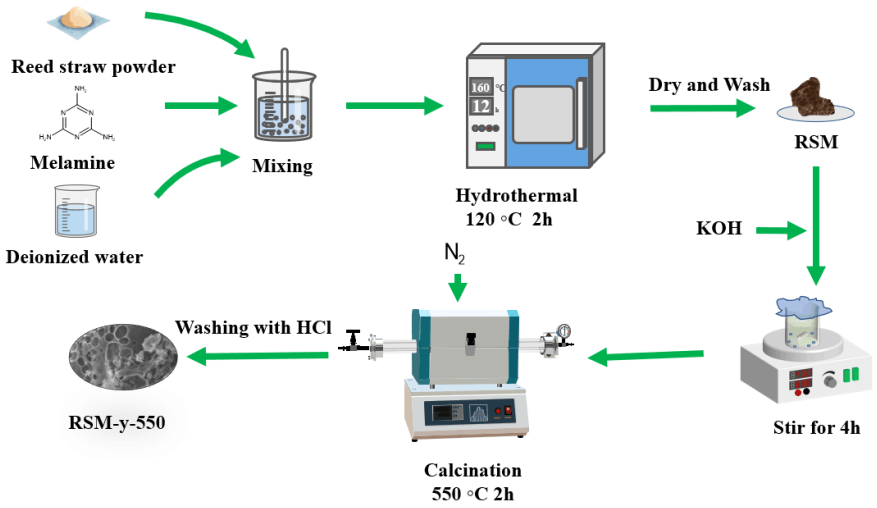

Figure 1. Schematic illustration of the synthesis procedure of the RSM-y-5.

3. Results and Discussion

Figure 1 shows the schematic illustration of the preparation process of the RSM-y-5. The reed straw powder and melamine were firstly mixed as the carbon and the nitrogen resource, respectively. Subsequently, the mixture was further pyrolysis under N_2 atmosphere with the KOH as the activator. Finally, the N-doped porous carbon was collected by after washing with HCl to remove the impurity. Figure 2 shows the SEM images of different RSM-y-550 samples (y = 0, 0.33, 1, and 3). The low-magnification SEM images of all samples shows irregular particle morphology, implying the defected structure of carbon material after pyrolysis and activation process. Figure 2a,b show the SEM images of RSM-0-550 sample without melamine addition. After introduction of melamine, no obvious change of morphology is observed (Figure 2c–h). Notably, some macropore structure can be found from the high-magnification SEM images for the RSM-0.33-550 (Figure S1a) and RSM-1-550 (Figure S2a) samples, and such macropore is conductive to the ion transport in electrolyte. In addition, the effect

 doi:10.20944/preprints202305.1311.v1

of activation temperature on the morphology of carbon is also investigated. For simplification, the as-prepared carbon materials were name as the RSM-1-x, and the x presents the value of the pyrolysis temperature of 400, 500, 550, 600, and 650 °C. As shown in Figure S2, the morphology of carbon material shows a more disorder and porous structure with the increased of activation temperature, which implies that higher pyrolysis temperature is favorable to the formation of porous structure.

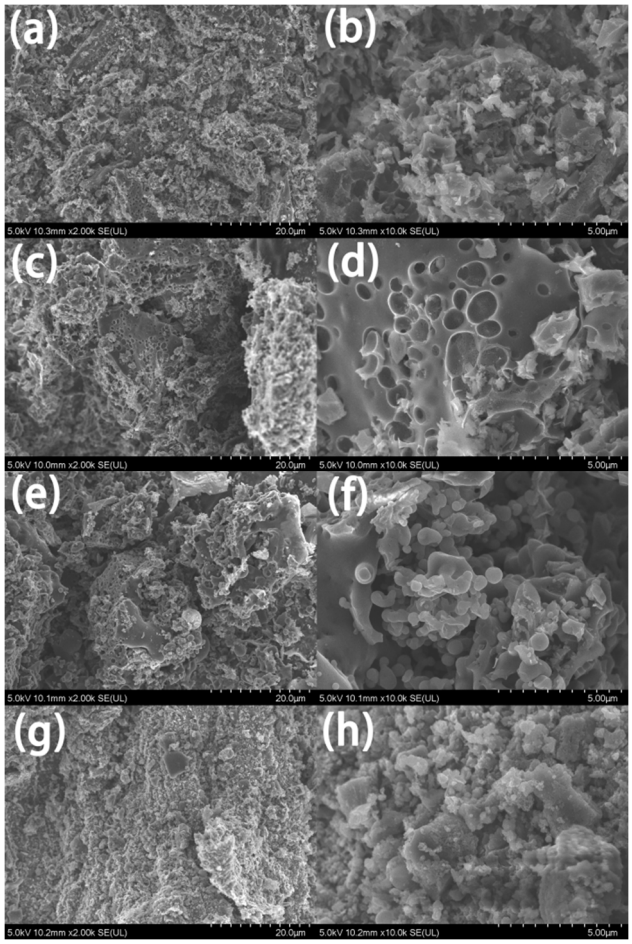

Figure 2. SEM image of reed straw based carbon material: (a, b) RSM-0-550, (c, d) RSM-0.33-550, (e, f) RSM-1-550, and (g, h) RSM-3-550.

Figure 3a clearly shows the XRD pattern of RSM-y-550. It can be observed that all the XRD patterns show a broad peak at 25 °, which corresponds to the typical feature of amorphous carbon [31]. Additionally, no characteristic peak of C_3N_4 derived from melamine is found [32,33]. Figure 3b shows the Raman spectra of a series of RSM-y-550 samples. Two obvious peaks are observed at 1363 and 1596 cm^{-1}, corresponding to G and D bands, respectively [34]. D band is related to the graphitic defective and disordered carbon structure, while G band is associated with to the E_{2g} symmetry between graphitic layers, which indicates ordered carbon structure [35]. The intensity ratio of G to D band (I_G/I_D) for all samples are illustrated as shown in Figure 3b. With the increased melamine addition, I_G/I_D decreased from 1.310 to 1.232, indicating a more disorder of the carbon structure. This could be conducive to the diffusion of electrolyte ions and the improvement of EDLC. It is worth noting that the value of I_G/I_D is 1.324 for RSM-3-550 sample, which suggests that the excessive addition of melamine increased the degree of carbon graphitization. This could be due to the formation of C_3N_4 after excessive melamine introduction. In addition, Figure S3a shows the XRD patterns of RSM-1-x obtained at different pyrolysis temperature, and similar results are observed. The Raman spectra of RSM-1-x are displayed in Figure S3b. Notably, with the increased activation temperature from 400 to 600 °C, the value of I_G/I_D decreased from 1.466 to 1.185. This indicates the higher temperature is conductive to the activation process, thus providing more interface of electrode and electrolyte.

Preprints (www.preprints.org) | NOT PEER-REVIEWED | Posted: 18 May 2023 doi:10.20944/preprints202305.1311.v1

However, the increased value of I_G/I_D of 1.213 is observed for RSM-1-650 sample, which could be attributed to the enhanced degree of graphitization at a higher pyrolysis temperature.

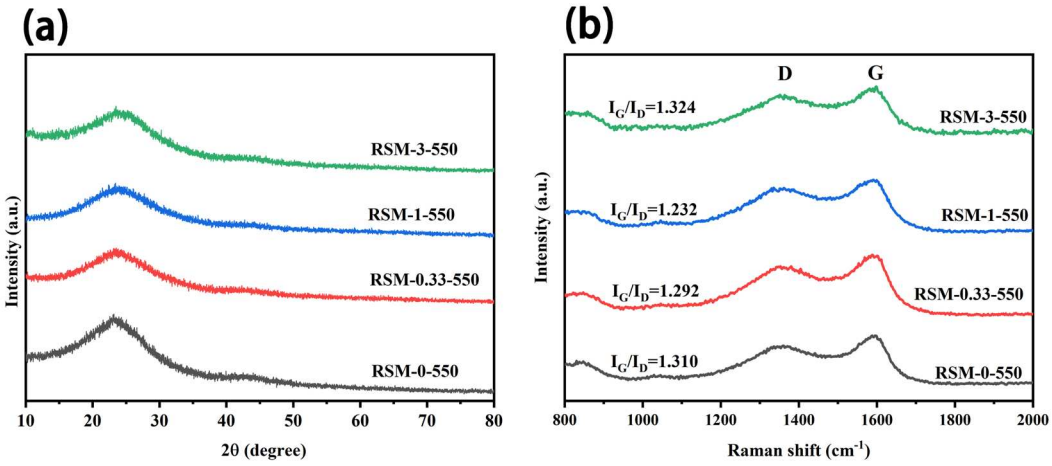

Figure 3. (a) XRD patterns of RSM-y-550 (y = 0, 0.33, 1, and 3), and (b) Raman spectra of RSM-y-550 (y = 0, 0.33, 1, and 3).

The wide scan XPS spectrum of RSM-0-550 (Figure 4a) shows the existence of C, N, and O elements, and the content was measured to be 81.1%, 5.2% and 13.6%, respectively. The existence of N element is ascribed to the protein from the reed straw [36]. After melamine addition, the obtained RSM-0.33-550 presents a N content of 6.1%, suggesting the N introduction (Figure 4d) [37]. Figure 4b and 4e compare the C 1s core-level XPS spectra of the RSM-0-550 and RSM-0.33-550 samples. Four peaks at 284.8, 286.1, 287.6, and 289.2 eV are observed, corresponding to the C-C/C=C, C-N/C-O, C=O, and O=C-O, respectively [38,39]. Notably, a little decline content of C-C and a small increase of C-N are observed for RSM-0.33-550 compared with RSM-0-550, implying that a part of the C-N bond replaced the C-C bond after melamine introducing. The N 1s XPS spectra of RSM-0-550 (Figure 4c) and RSM-0.33-550 (Figure 4f) display the four peaks at 398.6, 400.1, 401.3 and 405.6 eV, corresponding to the Pyridinic-N (N-6), Pyrrolic-N (N-5), Graphitic-N (G-N), and N-Oxide (N-O), respectively [11,40]. The relative densities of these N species can be illustrated from the proportional areas of corresponding peaks as displayed in Figure S4. It is well known that the N-6 presents more active compared with the other types of N, due to it can give more active sties and sufficient defects, and is more energetically favorable towards promoting the interaction between the electrode and electrolyte ions (alkali metal ions) [41]. Clearly, the content of N-6 increased from 15.4% to 24.8% after melamine introducing, indicating the increased active sites for charge storage. Moreover, the decline content of G-N from 14.9% to 10.3% after melamine introducing implies the more exposed edge sites, which can be due to the pyrolysis and activation process of melamine [42]. The N doping can considerably boost the performance of SCs by tunning the electronic conductivity, surface accessibility, and faradaic reaction. In the carbon framework, the N and C atoms with multi-graded elecronegativities give a polarized/accessible electrode surface with enhanced elecrosorption active sites for improved electrolyte-electrode interaction. Additionally, the boosted adsorption of alkali metal ions can be achieved on the N faradaic-active sites, resulting in good pseudocapacitance by electrochemical redox reactions [43,44].

Preprints (www.preprints.org) | NOT PEER-REVIEWED | Posted: 18 May 2023 doi:10.20944/preprints202305.1311.v1

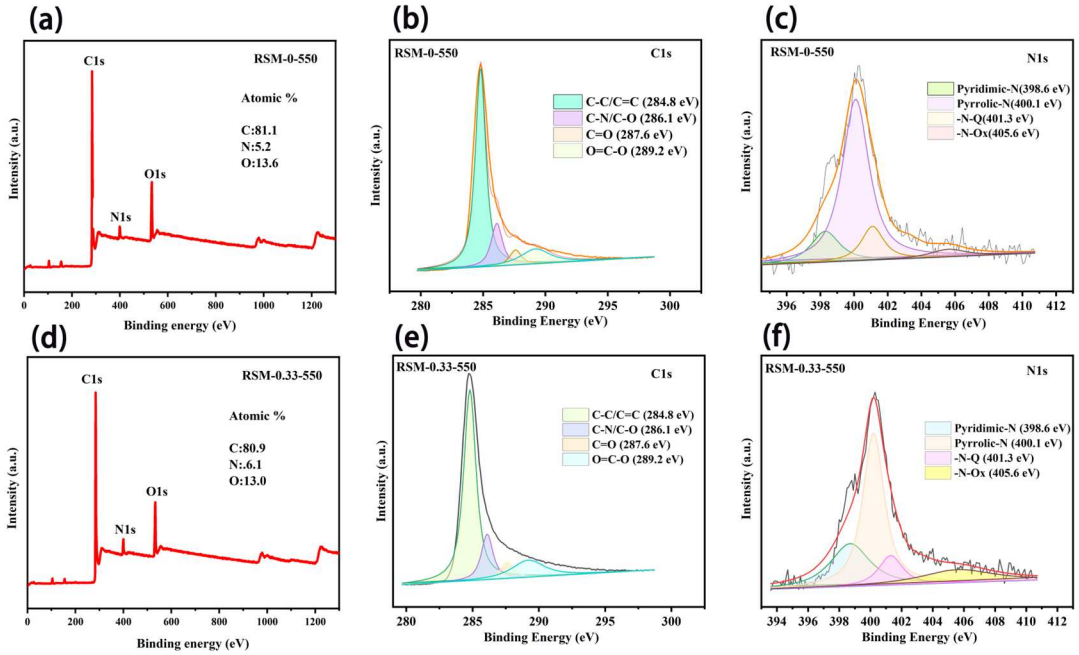

Figure 4. Wide scan XPS spectrum of (a) RSM-0-550. XPS spectra of RSM-0-550 for (b) C 1s and (c) N 1s regions. Wide scan XPS spectrum of (d) RSM-0.33-550. XPS spectrum of RSM-0.33-550 for (e) C 1s and (f) N 1s regions.

To study the porosity of the carbon materials, BET measurement was conducted. As displayed in Figure 5a, N_2 adsorption-desorption isotherms of RSM-0.33-550 displays the sharply rise adsorption quantity at $P/P_0 < 0.05$, indicating the type I (IUPAC classification) feature for microporous materials [45]. Clearly, the obvious hysteresis loop at $P/P_0 = 0.45–0.9$ and sharply increased at $P/P_0 = 0.9–1.0$ are found, indicates the existence of both meso- and microporous stricture in RSM-0.33-550 [42]. Figure 5b shows the corresponding pore size distribution, and the mesopores and micropores with the diameters of around 1.0 and 2.3 nm are achieved, respectively. The mesoporous pores have a positive effect on the charge storage, which is important for reaching high capacitance [35]. The detailed parameters are shown in Table S1, and it evidently shows that the surface area of RSM-0.33-550 is 547.1 $m^2\ g^{-1}$ with a pore volume of 0.159 $cm^3\ g^{-1}$. Therefore, this hierarchical porosity of such RSM-0.33-550 can give an abundant surface area and rapid electrolyte ions transfer for energy storage.

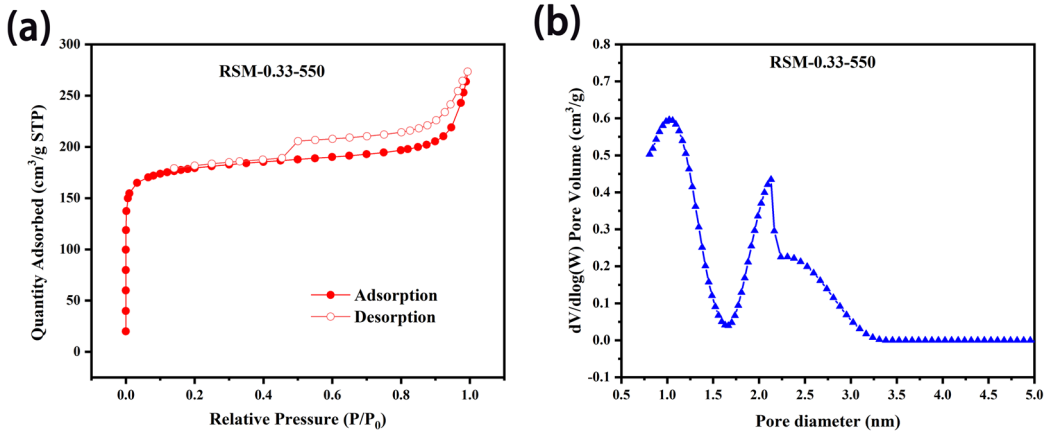

Figure 5. (a) N_2 adsorption and desorption isothermal curves of RSM-0.33-550, and (b) the corresponding pore size distributions.

 doi:10.20944/preprints202305.1311.v1

The electrochemical performance of all samples was evaluated by a three-electrode system, in which 6 M KOH was employed as the electrolyte due to its a higher ionic conductivity and a smaller radius of the hydration sphere (3.00 Å for OH^- and 3.31 Å for K^+). Figure S5 shows the GCD curves of RSM-1-x prepared by the different pyrolysis temperature. Clearly, the RSM-1-400, RSM-1-500, RSM-1-550, RSM-1-600, and RSM-1-650 electrode delivered a capacitance of 45.6, 145.4, 164.7, 146.3, and 120.1 F g^{-1}, respectively. Based on the GCD data, the related rate performance was illustrated in Figure S6. In addition, Figure S7 illustrates the CV curves of the RSM-1-y electrode, similar results were found. As shown in Figure S7f, the capacitance of 42.3, 131.2, 153.4, 142, and 114.9 F g^{-1} was achieved for RSM-1-400, RSM-1-500, RSM-1-550, RSM-1-600, and RSM-1-650 electrode, respectively. Notably, the CV curves of RSM-1-550, RSM-1-600, and RSM-1-650 electrodes (Figure S7c,d) show a relative quasi-rectangle shape compared with the RSM-1-400 and RSM-1-500, which is ascribed to that a higher pyrolysis temperature can provide a sufficient activation process, thus offering capacitive behavior for charge storage. This indicates that the activation temperature has a great influence on the electrochemical performance, which is manly ascribed to the change of the structure and surface chemistry of carbon materials.

Figure 6a summarizes the GCD curve of RSM-y-550 electrode at a current density of 1 A g^{-1}. All GCD curves present a relatively symmetrical profile, indicating the good coulombic efficiency and capacitive properties. Notably, RSM-0.33-550 electrode exhibited a longer discharge time, which implies its superior capacitance. The specific capacitance of RSM-0-550, RSM-0.33-550, RSM-1-550, and RSM-3-550 was calculated to be 181.6, 202.8, 164.7, and 159.3 F g^{-1}, respectively. This indicates that the rational melamine introduction is more beneficial to improve the electrochemical performance. The GCD cures of RSM-y-550 at different current densities are shown in Figure 6b and S8a–S8d. All GCD curves show the symmetrical triangle shape, indicating the good capacitive behavior. The corresponding rate performance based on GCD data is displayed in Figure 6c. Clearly, RSM-0.33-550 delivered a superior rate performance with a capacitance of 202.8, 194.4, 185.5, and 177, F g^{-1} at 1, 2, 5, and 10 A g^{-1}. Even at a current density of 20 A g^{-1}, a capacitance of 164 mF g^{-1} can be achieved, which is higher than that of RSM-0-550 (148 F g^{-1}), RSM-0-550 (120 F g^{-1}), and RSM-0-550 (98 F g^{-1}). In addition, the GCD curves of RSM-y-550 were also given in Figures 6d and S9. The capacitance of 171.2, 189.7, 153.4, and 146.3 F g^{-1} was reached for RSM-0-550, RSM-0.33-550, RSM-1-550, and RSM-3-550, respectively. More comparisons are listed in Table S2, and this indicates the superior electrochemical performance of RSM-0.33-550. Furthermore, EIS measurement was employed as shown in Figure 6e. The Nyquist plots of the RSM-0-550, RSM-0.33-550, and RSM-1-550 displayed a small semi-circle in the high frequency region, indicating their low charge transport resistance [46]. On the contrary, the Nyquist plot of RSM-3-550 presents a larger semicircle at high frequency region. The increased charge transport resistance could be ascribed to the formation of C_3N_4 derived from melamine after introducing excessive N resource [47]. At the low frequency region, it can be seen that RSM-0.33-550 has a highest slope, indicating that the electrolyte ion diffusion of RSM-0.33-550 is the most active and can provide faster current response. Figure 6f shows the long cycling test of RSM-0.33-550 electrode. Notably, it exhibited a good cycle stability with a capacitance retention rate of 96.3% (158 F g^{-1}) at a current density of 20 A g^{-1} after 5000 cycles.

Preprints (www.preprints.org) | NOT PEER-REVIEWED | Posted: 18 May 2023 doi:10.20944/preprints202305.1311.v1

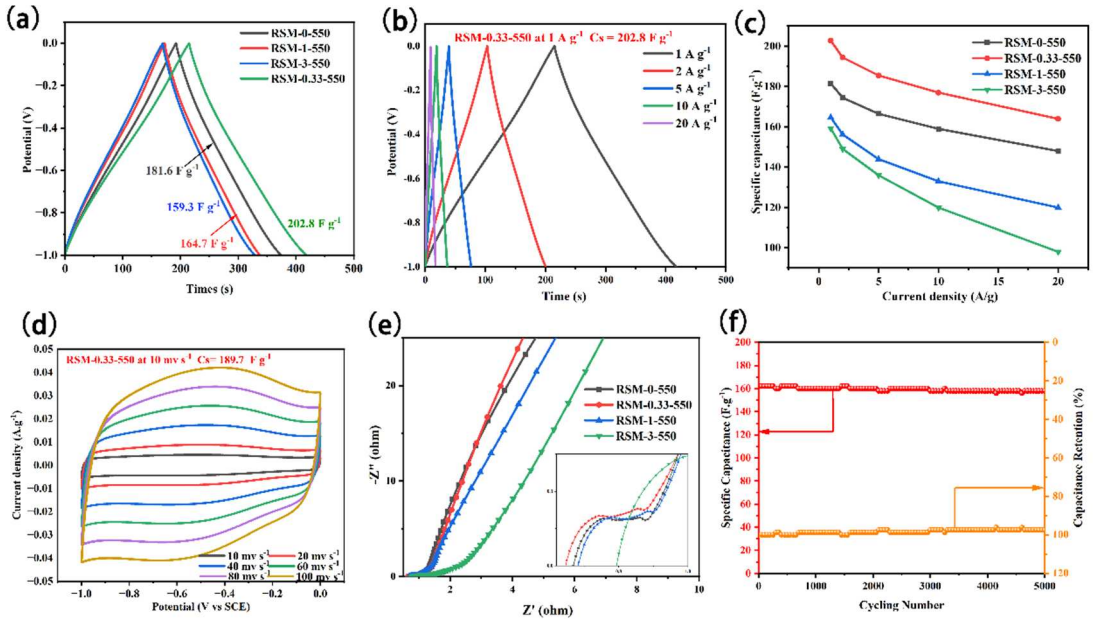

Figure 6. (a) GCD curves of all RSM-y-550 (y = 0, 0.33, 1, and 3) electrodes at a current density of 1 A g^{-1}. (b) GCD curves of RSM-0.33-550 at various current densities. (c) Rate performance at the current density of 1, 2, 4, 5, 8 and 10 A g^{-1}. (d) CV curves of RSM-0.33-550 at various scan rates of 10-150 mV s^{-1}. (e) Nyquist plots of RSM-y-550 (y=0, 0.33, 1, and 3). (f) Long cycling test at a current density of 20 A g^{-1} after 5000 cycles.

4. Conclusions

In summary, we proposed an efficient route to prepare a N-doped carbon material by directly pyrolyzing reed straw and melamine. The pyrolysis temperature and the mount of activator were carefully investigated. The rational regulation of the activation temperature and the amount of N resource is significant for the electrochemical performance of reed-straw based electrode. The optimized RSM-0.33-550 prepared at 550 °C with a mass ratio of melamine to reed straw of 0.33 possessed a N content of 6.02% and a specific surface area of 547.1 m^2 g^{-1}. As the anode for SCs, such RSM-0.33-550 electrode delivered a higher capacitance of 202.8 F g^{-1} at a current density of 1 A g^{-1}. EIS measurement exhibited a faster ion transfer for the RSM-0.33-550 electrode. Even at a current density of 20 A g^{-1}, the RSM-0.33-550 electrode can achieve a capacitance of 164 mF g^{-1}, which is higher than that of RSM-0-550 (148 F g^{-1}), RSM-0-550 (120 F g^{-1}), and RSM-0-550 (98 F g^{-1}). Notably, the RSM-0.33-550 electrode showed an excellent cyclic stability with 96.3% capacitance retention after 5000 cycles. This work offers us a new insight for rationally utilizing the biomass waste to prepare the functionalized carbon materials and the related application.

Supplementary Materials: The following supporting information can be downloaded at: www.mdpi.com/xxx/s1, Figure S1. SEM images of (a) RSM-0.33-550 and (b) RSM-1-550.; Figure S2. SEM images of (a, b) RSM-1-400, (c, d) RSM-1-500, (e, f) RSM-1-550, (g, h) RSM-1-600, and (i, j) RSM-1-650.; Figure S3. (a) XRD patterns of RSM-1-x (x = 400, 500, 550, 600, and 650 °C), (b) Raman spectra of RSM-1-x (x = 400, 500, 550, 600, and 650 °C).; Figure S4. The content of different N species in RSM-0-550 and RSM-0.33-550.; Figure S5. GCD curves of (a) RMS-1-400, (b) RMS-1-500, (c) RMS-1-550, (d) RMS-1-600, and (e) RMS-1-650 electrodes at the current densities of 1, 2, 4, 5, and 10 A g^{-1}, respectively. (f) The specific capacitance of RSM-1-X (X = 400, 500, 550, 600, and 650) at a current density of 1 A g^{-1}.; Figure S6. Rate performance of RSM-1-X (X = 400, 500, 550, 600, and 650) electrodes.; Figure S7. CV curves of (a) RSM-1-400, (b) RSM-1-500, (c) RSM-1-550, (d) RSM-1-600, and (e) RSM-1-650 electrodes at a scan rate of 10–150 mV s^{-1}. (e) The specific capacitance values of RSM-1-X (X = 400, 500, 550, 600, and 650) at a scan rate of 10 mV s^{-1}.; Figure S8. GCD curves of (a) RMS-0-550, (b) RMS-0.33-550, (c) RMS-1-550, and (d) RMS-3-550 electrodes at different current densities of 1, 2, 4, 5, and 10 A g^{-1}.; Figure S9. CV curves of (a) RMS-0-550, (b) RMS-0.33-550, (c) RMS-1-550, and (d) RMS-3-550 electrodes at a scan rate of 10–150 mV s^{-1}.; Table S1. structural parameters of RSM-0.33-550.; Table S2. Electrochemical performance of RSM-0.33-550 and reported carbonaceous materials electrode in supercapacitors.

Author Contributions: Conceptualization, S.Y. and Y.W.; methodology, S.Y.; software, Y.W.; validation, S.Y., Y.W. and Y.L.; formal analysis, Y.L.; investigation, Y.L.; resources, Z.S.; data curation, G.J., D.W. and Q.Y; writing—original draft preparation, Y.L., Z.S., G.J. and Y.W; writing—review and editing, Y.W. and S.Y.; visualization, Y.W.; supervision, S.Y.; project administration, S.Y.; funding acquisition, S.Y. All authors have read and agreed to the published version of the manuscript.

Funding: This research was funded by the National Natural Science Foundation of China (No. 2197812)

Institutional Review Board Statement: Not applicable.

Informed Consent Statement: Not applicable.

Data Availability Statement: Data are contained within the article.

Acknowledgments: The authors are appreciative of the funds granted by the National Natural Science Foundation of China (No. 21978182). The authors also acknowledge Dr. Xiang Lin, Dr. Ji Li, Mr. Pan Wu and Dr. Jie Wei from the Engineering Teaching Center, School of Chemical Engineering, Sichuan University and Dr. Yingming Zhu from the Institute of New Energy and Low Carbon Technology of Sichuan University for the XRD, Raman, and SEM measurement, and Miss Panpan Li from Shiyanjia Lab (www.shiyanjia.com) for XPS measurement.

Conflicts of Interest: The authors declare no conflict of interest.

Sample Availability: The Samples are available from the authors.

References

1. Chu, S.; Majumdar, A., Opportunities and challenges for a sustainable energy future. Nature 2012, 488, 294-303.
2. Wang, Y.; Wu, C.; Wu, Z.; Cui, G.; Xie, F.; Guo, X.; Sun, X., FeP nanorod arrays on carbon cloth: a high-performance anode for sodium-ion batteries. Chemical Communications 2018, 54, 9341-9344.
3. Muzaffar, A.; Ahamed, M. B.; Deshmukh, K.; Thirumalai, J., A review on recent advances in hybrid supercapacitors: Design, fabrication and applications. Renewable and Sustainable Energy Reviews 2019, 101, 123-145.
4. Simon, P.; Gogotsi, Y., Materials for electrochemical capacitors. Nature Materials 2008, 7, 845-854.
5. Pohlmann, S., Metrics and methods for moving from research to innovation in energy storage. Nature Communications 2022, 13, 1538.
6. Tang, J.; Yuan, H.; Duan, Q.; Liu, Y.; Wang, Y.; Yuan, S., Phosphorus-functionalized low-crystallinity transition-metal oxide nanorod arrays grown on carbon cloth for high-performance asymmetric supercapacitors. Colloids and Surfaces A: Physicochemical and Engineering Aspects 2022, 654, 130189.
7. Wu, C.; Pei, Z.; Lv, M.; Huang, D.; Wang, Y.; Yuan, S., Polypyrrole-coated low-crystallinity iron oxide grown on carbon cloth enabling enhanced electrochemical supercapacitor performance. Molecules, 2023, 28, 434.
8. Tang, H.; Yao, J.; Zhu, Y., Recent developments and future prospects for zinc-ion hybrid capacitors: a review. Advanced Energy Materials 2021, 11, 2003994.
9. Yuan, Y.; Huang, L.; Yılmaz, M.; Zhang, T. C.; Wang, Y.; Yuan, S., $MgFe_2O_4$-loaded N-doped biochar derived from waste cooked rice for efficient low-temperature desulfurization of H_2S. Fuel 2023, 339, 127385.
10. Huang, L.; Liu, H.; Wang, Y.; Zhang, T. C.; Yuan, S., Construction of ternary Bi_2O_3/biochar/g-C_3N_4 heterojunction to accelerate photoinduced carrier separation for enhanced tetracycline photodegradation. Applied Surface Science 2023, 616, 156509.
11. Wang, Y.; Zhang, T.; Xiao, J.; Tian, X.; Yuan, S., Enhancing electrochemical performance of ultrasmall Fe_2O_3-embedded carbon nanotubes via combusting-induced high-valence dopants. Journal of Materials Science & Technology 2023, 134, 142-150.
12. Xiao, J.; Zhang, Y.; Zhang, T. C.; Yuan, S., Prussian blue-impregnated waste pomelo peels-derived biochar for enhanced adsorption of NH_3. Journal of Cleaner Production 2023, 382, 135393.
13. Yuan, Y.; Huang, L.; Zhang, T. C.; Ouyang, L.; Yuan, S., One-step synthesis of $ZnFe_2O_4$-loaded biochar derived from leftover rice for high-performance H_2S removal. Separation and Purification Technology 2021, 279, 119686.

14. Momodu, D.; Madito, M.; Barzegar, F.; Bello, A.; Khaleed, A.; Olaniyan, O.; Dangbegnon, J.; Manyala, N., Activated carbon derived from tree bark biomass with promising material properties for supercapacitors. Journal of Solid State Electrochemistry 2017, 21, 859-872.
15. Kesavan, T.; Raaju Sundhar, A. S.; Dharaneshwar, S.; Prabu, N.; Manickam, S., N-Doped carbon nanosheets from biomass for ultra long-cycling and high energy density symmetric supercapacitors. ECS Journal of Solid State Science and Technology 2021, 10, 051004.
16. Taer, E.; Apriwandi, A.; Febriani, W.; Taslim, R., Suitable micro/mesoporous carbon derived from galangal leaves (Alpinia galanga L.) biomass for enhancing symmetric electrochemical double-layer capacitor performances. ChemistrySelect 2022, 7, e202201810.
17. Kang, W.; Lin, B.; Huang, G.; Zhang, C.; Yao, Y.; Hou, W.; Xu, B.; Xing, B., Peanut bran derived hierarchical porous carbon for supercapacitor. Journal of Materials Science: Materials in Electronics 2018, 29, 6361-6368.
18. Dai, C.; Wan, J.; Shao, J.; Ma, F., Hollow activated carbon with unique through-pore structure derived from reed straw for high-performance supercapacitors. Materials Letters 2017, 193, 279-282.
19. Xie, Q.; Zheng, A.; Zhai, S.; Wu, S.; Xie, C.; Zhang, Y.; Guan, Y., Reed straw derived active carbon/graphene hybrids as sustainable high-performance electrodes for advanced supercapacitors. Journal of Solid State Electrochemistry 2016, 20, 449-457.
20. Chodankar, N. R.; Ji, S.; Han, Y.; Kim, D., Dendritic nanostructured waste copper wires for high-energy alkaline battery. Nano-Micro Letters 2019, 12, 1.
21. Wei, Q.; Chen, Z.; Cheng, Y.; Wang, X.; Yang, X.; Wang, Z., Preparation and electrochemical performance of orange peel based-activated carbons activated by different activators. Colloids and Surfaces A: Physicochemical and Engineering Aspects 2019, 574, 221-227.
22. Tian, Q.; Wang, X.; Xu, X.; Zhang, M.; Wang, L.; Zhao, X.; An, Z.; Yao, H.; Gao, J., A novel porous carbon material made from wild rice stem and its application in supercapacitors. Materials Chemistry and Physics 2018, 213, 267-276.
23. Deng, J.; Xiong, T.; Xu, F.; Li, M.; Han, C.; Gong, Y.; Wang, H.; Wang, Y., Inspired by bread leavening: one-pot synthesis of hierarchically porous carbon for supercapacitors. Green Chemistry 2015, 17, 4053-4060.
24. Gao, Y.; Zhang, Y.; Li, A.; Zhang, L., Facile synthesis of high-surface area mesoporous biochar for energy storage via in-situ template strategy. Materials Letters 2018, 230, 183-186.
25. Wang, Y.; Xiao, J.; Zhang, T.; Ouyang, L.; Yuan, S., Single-step preparation of ultrasmall iron oxide-embedded carbon nanotubes on carbon cloth with excellent superhydrophilicity and enhanced supercapacitor performance. ACS Applied Materials & Interfaces 2021, 13, 45670-45678.
26. Xiao, J.; Wang, Y.; Zhang, T. C.; Ouyang, L.; Yuan, S., Phytic acid-induced self-assembled chitosan gel-derived N, P–co-doped porous carbon for high-performance CO_2 capture and supercapacitor. Journal of Power Sources 2022, 517, 230727.
27. Xiao, J.; Wang, Y.; Zhang, T. C.; Yuan, S., N,S-containing polycondensate-derived porous carbon materials for superior CO_2 adsorption and supercapacitor. Applied Surface Science 2021, 562, 150128.
28. Zhang, Y.; Xiao, J.; Zhang, T. C.; Ouyang, L.; Yuan, S., Synthesis of $CuSiO_3$-loaded P-doped porous biochar derived from phytic acid-activated lemon peel for enhanced adsorption of NH_3. Separation and Purification Technology 2022, 283, 120179.
29. Feng, X.; Bai, Y.; Liu, M.; Li, Y.; Yang, H.; Wang, X.; Wu, C., Untangling the respective effects of heteroatom-doped carbon materials in batteries, supercapacitors and the ORR to design high performance materials. Energy & Environmental Science 2021, 14, 2036-2089.
30. Xiao, J.; Wang, Y.; Zhang, T. C.; Yuan, S., rGO/N-porous carbon composites for enhanced CO_2 capture and energy storage performances. Journal of Alloys and Compounds 2021, 857, 157534.
31. Yuan, X.; Xiao, J.; Yılmaz, M.; Zhang, T. C.; Yuan, S., N, P Co-doped porous biochar derived from cornstalk for high performance CO_2 adsorption and electrochemical energy storage. Separation and Purification Technology 2022, 299, 121719.
32. Liu, H.; Huo, W.; Zhang, T. C.; Ouyang, L.; Yuan, S., Photocatalytic removal of tetracycline by a Z-scheme heterojunction of bismuth oxyiodide/exfoliated g-C_3N_4: performance, mechanism, and degradation pathway. Materials Today Chemistry 2022, 23, 100729.
33. Yoon, Y.; Lee, M.; Kim, S. K.; Bae, G.; Song, W.; Myung, S.; Lim, J.; Lee, S. S.; Zyung, T.; An, K.-S., A strategy for synthesis of carbon nitride induced chemically doped 2D MXene for high-performance Supercapacitor Electrodes. Advanced Energy Materials 2018, 8, 1703173.

34. Szubzda, B.; Szmaja, A.; Halama, A., Influence of structure and wettability of supercapacitor electrodes carbon materials on their electrochemical properties in water and organic solutions. Electrochimica Acta 2012, 86, 255-259.
35. Wang, Y.; Wang, H.; Zhang, T. C.; Yuan, S.; Liang, B., N-doped porous carbon derived from rGO-Incorporated polyphenylenediamine composites for CO_2 adsorption and supercapacitors. Journal of Power Sources 2020, 472, 228610.
36. Wang, Q.; Juan, J.; Xiao, T.; Zhang, J.; Chen, H.; Song, X.; Chen, M.; Huang, J., The physical structure of compost and C and N utilization during composting and mushroom growth in Agaricus bisporus cultivation with rice, wheat, and reed straw-based composts. Applied Microbiology and Biotechnology 2021, 105, 3811-3823.
37. Fan, X.; Tan, F.; Meng, F.; Liu, J., Hierarchical porous N-doped carbon nanosheets obtained by organic–inorganic bipolymeric engineering for improved lithium–sulfur batteries. Chemistry – A European Journal 2019, 25, 4040-4046.
38. Wang, Y.; Zhang, P.; Zhang, T. C.; Xiang, G.; Wang, X.; Pehkonen, S.; Yuan, S., A magnetic γ-Fe_2O_3@PANI@TiO_2 core–shell nanocomposite for arsenic removal via a coupled visible-light-induced photocatalytic oxidation–adsorption process. Nanoscale Advances 2020, 2, 2018-2024.
39. Wang, Y.; Zhang, Y.; Zhang, T. C.; Xiang, G.; Wang, X.; Yuan, S., Removal of trace arsenite through simultaneous photocatalytic oxidation and adsorption by magnetic Fe_3O_4@PpPDA@TiO_2 core–shell nanoparticles. ACS Applied Nano Materials 2020, 3, 8495-8504.
40. Wang, Y.; Du, Z.; Xiao, J.; Cen, W.; Yuan, S., Polypyrrole-encapsulated Fe_2O_3 nanotube arrays on a carbon cloth support: Achieving synergistic effect for enhanced supercapacitor performance. Electrochimica Acta 2021, 386, 138486.
41. He, H.; Huang, D.; Tang, Y.; Wang, Q.; Ji, X.; Wang, H.; Guo, Z., Tuning nitrogen species in three-dimensional porous carbon via phosphorus doping for ultra-fast potassium storage. Nano Energy 2019, 57, 728-736.
42. Wang, Y.; Xiao, J.; Wang, H.; Zhang, T. C.; Yuan, S., Binary doping of nitrogen and phosphorus into porous carbon: A novel di-functional material for enhancing CO_2 capture and super-capacitance. Journal of Materials Science & Technology 2022, 99, 73-81.
43. He, H.; Gan, Q.; Wang, H.; Xu, G.-L.; Zhang, X.; Huang, D.; Fu, F.; Tang, Y.; Amine, K.; Shao, M., Structure-dependent performance of TiO_2/C as anode material for Na-ion batteries. Nano Energy 2018, 44, 217-227.
44. Wu, Y.; Jiang, Y.; Shi, J.; Gu, L.; Yu, Y., Multichannel porous TiO_2 hollow nanofibers with rich oxygen vacancies and high grain boundary density enabling superior sodium storage performance. Small 2017, 13, 1700129.
45. Wang, Y.; Xiao, J.; Wang, H.; Zhang, T. C.; Yuan, S., N-doped porous carbon derived from solvent-free synthesis of cross-linked triazine polymers for simultaneously achieving CO_2 capture and supercapacitors. Chemistry–A European Journal 2021, 27, 7908-7914.
46. Wang, Y.; Jia, K.; Pan, Q.; Xu, Y.; Liu, Q.; Cui, G.; Guo, X.; Sun, X., Boron-doped TiO_2 for efficient electrocatalytic N_2 fixation to NH_3 at ambient conditions. ACS Sustainable Chemistry & Engineering 2019, 7, 117-122.
47. Zhang, J.; Pan, L.; Zhang, X.; Shi, C.; Zou, J., Donor-acceptor carbon nitride with electron-withdrawing chlorine group to promote exciton dissociation. Chinese Journal of Catalysis 2021, 42, 1168-1175.